

# Imaging polarimetry of stellar light scattered in detached shells around the carbon stars R Scl and U Ant<sup>★</sup>

D. González Delgado<sup>1</sup>, H. Olofsson<sup>1</sup>, H. E. Schwarz<sup>2</sup>, K. Eriksson<sup>3</sup>, B. Gustafsson<sup>3</sup>, and T. Gledhill<sup>4</sup>

<sup>1</sup> Stockholm Observatory, SCFAB, 106 91 Stockholm, Sweden

<sup>2</sup> CTIO, Casilla 603, La Serena, Chile

<sup>3</sup> Uppsala Astronomical Observatory, Box 515, 751 20 Uppsala, Sweden

<sup>4</sup> Department of Physical Sciences, University of Hertfordshire, College Lane, Hatfield, Hertfordshire AL10 9AB, UK

Received 11 June 2002 / Accepted 30 October 2002

**Abstract.** Imaging polarimetry has been used to study the extended, detached circumstellar shells around the bright carbon stars R Scl and U Ant. The observations were done in two narrow band filters centred on the resonance lines of neutral K and Na, but much broader than the expected line widths. The polarimetric data reveal brightness distributions, in both cases, which are in perfect agreement with previous observations of scattered light obtained through direct imaging techniques. The total intensity images towards R Scl outline, in both filters, circular disk-like distributions out to a radius of  $\approx 21''$ , where the intensity drops sharply. The polarised intensity images reveal, however, that the scattering occurs in a geometrically thin shell. The degree of polarisation reaches values of  $\approx 35\%$  in both filters. The imaging polarimetry observations of U Ant reveal a somewhat more complex structure, where the existence of several shells can be discerned. The polarised scattered light comes from a component, at a radius of  $\approx 50''$  from the star, which lies outside the region where the bulk of the light is scattered. The latter comes from a dominating shell at  $\approx 43''$ , which coincides spatially with the detached gas shell inferred from CO radio line data, and there may be another two shells inside this. The polarisation degree reaches  $\approx 50\%$  in the outer component. We model, with a code based on the Monte Carlo method, the scattered emission under the assumption of dust scattering, using the observed polarised brightness distributions as constraints. In the case of R Scl we found that the polarised, as well as the total, light distributions can be explained by scattering in a  $2''$  wide shell of radius  $20''$  containing a dust mass of  $\approx 2 \times 10^{-6} M_{\odot}$ . This dust shell is also responsible for the thermal dust emission measured by IRAS. There is room, up to 30% of the total scattered flux, for other scattering agents. Comparison with CO radio line data shows that this dust shell probably lies outside the detached CO gas shell. In the case of U Ant the modelling explains the outer component in terms of a  $5''$  wide shell at a radius of about  $52''$  with a dust mass of  $\approx 4 \times 10^{-6} M_{\odot}$ . This is also the dust shell responsible for the emission measured by IRAS. However, the bulk of the scattered light cannot in this case be due to scattering by dust. In accordance with a discussion in a previous paper we attribute the remaining, unpolarised, scattering to the KI and NaD resonance lines. In both cases we found evidence that a dust shell has separated from the rest of the circumstellar medium. This may be due to gas-grain drift, or to hydrodynamical effects, which may also explain the complex multiple-shell structure seen towards U Ant. The model results are very dependent on the grain size distribution, and the observational data can only be reconciled with a very steep decline in grain size.

**Key words.** stars: carbon – circumstellar matter – polarization – stars: individual: R Scl, U Ant – stars: mass-loss

## 1. Introduction

The circumstellar envelopes (CSEs) of asymptotic giant branch (AGB) stars are the results of extensive stellar mass loss. This is one of the most important processes affecting the final evolution of low- and intermediate-mass stars. The CSEs may also be one of the principal seed beds for the formation of (more or

less) complex molecules and dust grains, and they are among the main contributors to the (nuclear-processed) gas mass return in the Galaxy. Hence, an understanding of the circumstellar environment is astrophysically very important (Olofsson 1999). Even though the general phenomenon of mass loss on the AGB is well established there remains a number of unsolved problems. One of them is the temporal variations of the mass loss on different time scales, and the mechanisms responsible for this. In this paper we are concerned with variations in individual stars on time scales of  $\lesssim 10^3$  to about  $10^4$  years.

Send offprint requests to: D. González Delgado,  
e-mail: delgado@astro.su.se

<sup>★</sup> Based on observations using the 3.6 m telescope of the European Southern Observatory, La Silla, Chile.

In a few cases, the circumstellar material has been observed in the form of completely detached gas/dust shells of large size,  $\gtrsim 10''$ . In particular, CO radio line observations reveal this phenomenon for a number of carbon stars: R Scl, U Ant, S Sct (Olofsson et al. 1996); TT Cyg (Olofsson et al. 1996, 2000); U Cam (Lindqvist et al. 1996, 1999). Also, detached dust shells have been detected around a handful of AGB and post-AGB stars (Waters et al. 1994; Izumiura et al. 1996, 1997; Hashimoto et al. 1998; Speck et al. 2000). In addition, multiple-shell structures have been seen in scattered light towards the high mass loss rate carbon star IRC+10216 and some post-AGB objects (Harpaz et al. 1997; Kwok et al. 1998; Sahai et al. 1998; Maunon & Huggins 1999, 2000). These data suggest more or less episodic mass loss on a number of different time scales (Olofsson et al. 1990; Schröder et al. 1999), and effects of interacting winds and interactions between gas and dust in winds may also be present (Olofsson et al. 2000; Steffen & Schönberner 2000; Simis et al. 2001).

In González Delgado et al. (2001, hereafter Paper I) we succeeded in imaging two of these detached shells in scattered stellar light, R Scl and U Ant; a novel way of obtaining independent data at an angular resolution much higher than that usually obtainable at radio wavelengths. The images exhibit brightness distributions in the form of relatively uniform-intensity disks, centred on the stars, with sharp outer radii at  $21''$  and  $43''$  in the case of R Scl and U Ant, respectively. For U Ant, the CO radio line data and the optical images are in good agreement in terms of the size of the detached shell, but the latter reveal new structures not present in the former. For R Scl the light appears to be scattered in a shell, which is significantly larger than the one detected in CO.

An interesting way of continuing this study is to obtain also polarimetric information on the scattered light. The advent of modern imaging techniques has opened up the possibility to obtain images in polarised light. Such data have been used to investigate the morphology of the CSE around IRC+10216 at infrared wavelengths. They show an axi-symmetric reflection nebula with the central star acting as the source of illumination (Tamura et al. 1988; Kastner & Weintraub 1994). Also, the light scattered in the extended dust envelopes around two supergiants,  $\alpha$  Ori and  $\mu$  Cep, taken in *UBV* filters, shows indications of polarisation (Le Borgne et al. 1986; Maunon & Le Borgne 1986; Le Borgne & Maunon 1989).

Imaging polarimetry has proven to be a very efficient observational mode for resolving the dust around bright central stars on small angular scales, regions usually unreachable by conventional imaging. Gledhill et al. (2001) used this technique in a study of a sample of proto-planetary nebulae (PPNe). It allowed them to classify the envelope morphologies on the basis of the polarisation characteristics. It is also a good tool for determining the position of the illuminating stars in PPNe. Thus, the presence of a self-luminous source in the centre of the Egg Nebula, as derived from direct and polarimetric images obtained with HST/NICMOS, led to the identification of a binary companion to the central star, which irradiates the nebula (Sahai et al. 1998; Weintraub et al. 2000).

In this paper we study the polarisation of optical light scattered in the circumstellar environments around the two carbon

stars presented in direct images in Paper I, R Scl and U Ant. For these objects the imaging polarimetry allows a further study of the nature of the scattered light and the structure of the shells.

## 2. Observations

### 2.1. Observational methods

The polarimetric observations of R Scl and U Ant were done in November 2000 and March 2001, respectively, with the EFOSC2 focal reducer camera on the ESO 3.6 m telescope. A summary of the observations is given in Table 1.

In all cases the observations were done through 5 nm FWHM filters centred on the resonance lines of NaI (589.0 nm and 589.6 nm; the *D* lines) [hereafter F59] and KI (769.9 nm) [hereafter F77]. These resonance lines, under the conditions commonly present in the CSEs around AGB stars, only cover a small fraction of the filter bandwidths. Therefore, observations taken in these filters contain information on the scattering by both the gas and the dust particles in the CSEs. These filters were chosen initially because spectroscopic observations showed the presence of extended circumstellar KI resonance line scattered light towards R Scl (Gustafsson et al. 1997). The subsequent observations reported in Paper I indicated a more complex situation where also dust scattering may contribute. Attempts to obtain images in standard filters, covering no strong spectral lines in AGB-CSEs, at the 3.6 m ESO telescope have proven to be difficult for our large dynamic range observations. Only in the Strömgren *b* filter was an acceptable image obtained (see Paper I). Therefore, we have continued to use our high-quality filters despite the difficulty to properly separate different scattering agents.

The energy flux of the stellar light scattered in the circumstellar medium is very low when compared to that of the central star. The images presented in Paper I show that they typically differ by (at least) a factor of  $10^3$ . In addition, the weak scattered light is spread over a sizeable area, substantially larger than the dominating part of the stellar point spread function (PSF), and long exposure times are required. Therefore, the use of a coronagraph is essential for separating the light scattered in the circumstellar medium from the direct strong stellar light which is scattered in the Earth's atmosphere and the telescope, and for allowing long exposure times, which would otherwise lead to a saturation in the CCD images. An important factor is the size of the coronagraphic mask to be used. The ideal occulting mask is small enough to allow detection of light scattered in regions close to the star, but large enough that the direct stellar flux does not dominate the detected light or saturate the detector in too short exposure times. Following several tests, we selected a coronagraphic mask of  $\approx 8''$  in radius for all observations. A Lyot stop was used to avoid the diffraction pattern of the telescope spiders.

Even the use of a coronagraph cannot eliminate the wings of the stellar PSF in the images, since the direct stellar light is scattered outside the coronagraphic mask by the Earth's atmosphere and the telescope. The presence of such a remaining stellar component in the images introduces difficulties when estimating the intensity distribution of the scattered light and it

**Table 1.** Observations performed with EFOSC2 on the ESO 3.6 m telescope.

Star	Epoch	Pixel size	Filters	Coronagraph	Template star
R Scl	Nov. 00	0'32	F59, F77	Needle mask	HR 4565
U Ant	March 01	0'32	F59, F77	Spot on kevlar spiders	HR 1877

needs to be removed. Images of stars of about the same spectral type and magnitude as our targets, but not showing scattered light of circumstellar origin, were observed regularly during the night to trace the time variations of the stellar PSFs due to changes in the atmospheric seeing and the telescope focus. The template stars are given in Table 1. In this way, the subtraction of any remnant of the stellar PSF in the image can be performed in a rather accurate fashion. The detailed procedure for removing the stellar PSF is described in Paper I. Note, however, that the images showing the polarimetric information of the scattered light do not contain any stellar component after reduction. They are obtained from the subtraction of observations taken at orthogonal polarisation angles, and therefore any remaining (unpolarised) stellar light is essentially cancelled out (see Sect. 3).

## 2.2. The instrumental setup for EFOSC2

The imaging polarimetry with EFOSC2 was done using a rotating half-wave plate and a fixed polaroid. By rotating the half-wave plate in steps of  $22.5^\circ$  we obtained images in linear polarisation with position angles in steps of  $45^\circ$ .

The observations of R Scl were done with a needle/spot coronagraph, which turned out to produce images less neat than expected due to diffraction along the supporting needle. For this reason, this coronagraph was replaced in the observations of U Ant by a small, black, metal disk supported by  $7\ \mu\text{m}$ -wide kevlar spiders.

The pixel plate scale of the images was set to  $0'.32/\text{pixel}$  by binning the images by a factor of two.

## 2.3. Data calibration

In a quantitative analysis of the scattered light, the calibration of the data is of course essential. A calibration in physical units requires observations of spectrophotometric standards. Although this was our goal, the weather conditions during the runs did not allow us to observe calibration standards. However, to study the nature of the detected light, it is often enough to estimate the total flux of the light scattered in the circumstellar medium relative to the stellar total flux (in CCD counts). This requires images of the target stars without the coronagraphic mask so that the stellar total fluxes can be derived. Due to different degrees of cloud cover during the runs we were not able to obtain such data.

Instead we used an indirect method for deriving the fluxes. The stellar flux densities were calculated based on published magnitudes. The variability of our targets ( $\approx 0.5$  mag at visual wavelengths) introduces some uncertainty in the calculation,

but the obtained values should be within a factor of two of the actual fluxes.

The scattered light fluxes were converted from CCD units to physical units in the following way. The counts/s were transformed to fluxes above the atmosphere by correcting for atmospheric absorption, telescope aperture with a central obstruction, telescope reflectivity, instrument transmission, filter bandpasses and transmission, and the quantum efficiencies and gains of the CCDs. This is the same approach as used in Paper I. A 20% uncertainty in the reflectivity, transmissions, efficiencies and gains, and a 50% uncertainty in the atmospheric absorption translate into scattered light fluxes that are accurate to within a factor of three. In all, we estimate that the ratios of the scattered flux (in the circumstellar medium) to the stellar flux given here are accurate to within a factor of five. It is important to emphasize that the ratios of polarised scattered flux to total scattered flux, i.e., the polarisation degrees, given here are relatively accurate, since they are estimated from the same images and hence are independent of the absolute calibration. An uncertainty in these ratios are introduced by the subtraction of the stellar PSF (see below), and we estimate that they are accurate to within 20%.

Furthermore, observations of spectropolarimetric standards are needed in imaging polarimetry in order to determine the polarisation introduced by the telescope and the instrument. Once again, such observations could not be done. Therefore, we were forced to neglect any instrumental polarisation. Finally, for an accurate calibration of the data one needs to observe regions close to the target stars in order to measure the sky polarisation, e.g., due to the presence of moonlight. We estimate that such polarisation has a negligible effect on our final results. Below we give some reasons which justify these assumptions, including the results from the observations of the template stars.

## 3. Data reduction

The large dynamic ranges of the images considerably complicate the data reduction. In particular, the difficulty lies in separating the contribution of the light scattered in the circumstellar medium from the stellar light scattered in the Earth's atmosphere and the telescope. The reduction of the direct images was described in some detail in Paper I. Here we concentrate on the reduction of the polarisation data. Due to time limitations during the observing runs, we observed the objects at only three polarisation angles ( $0^\circ$ ,  $45^\circ$ ,  $90^\circ$ ). The images were bias-subtracted, flatfield-corrected, and removed of cosmic ray hits using different IRAF tasks. For each target the exposures taken at a certain polarisation angle were aligned using stars in the FOV, and they were subsequently added to increase the S/N-ratio.

The measured Stokes parameters of the detected light ( $I_m$ ,  $Q_m$ ,  $U_m$ ) contain contributions from four components,

$$\begin{cases} I_m = I_* + I_{sc} + I_{sh} + I_{bg} \\ Q_m = Q_* + Q_{sc} + Q_{sh} + Q_{bg} \\ U_m = U_* + U_{sc} + U_{sh} + U_{bg}, \end{cases} \quad (1)$$

where ( $I_*$ ,  $Q_*$ ,  $U_*$ ) are due to the direct stellar light, ( $I_{sc}$ ,  $Q_{sc}$ ,  $U_{sc}$ ) are due to stellar light scattered in the interstellar medium, the Earth's atmosphere, and the telescope, ( $I_{sh}$ ,  $Q_{sh}$ ,  $U_{sh}$ ) are the intrinsic values of the stellar light scattered by the circumstellar medium, and ( $I_{bg}$ ,  $Q_{bg}$ ,  $U_{bg}$ ) are due to the sky background.

As we do not have polarimetric information on the target stars themselves, we have to assume that the photospheric stellar light is essentially unpolarised. The *BVRI* polarimetry study of a sample of ten carbon stars of different variability types done by Raveendran (1991) shows that the spatially unresolved light from these stars (and their envelopes) is only weakly polarised ( $\lesssim 1\%$ ). This value sets a very low upper limit to the intrinsic polarisation of the stellar radiation, i.e.,  $Q_* \approx 0$  and  $U_* \approx 0$ .

The high galactic latitudes of R Scl and U Ant, together with them being relatively nearby, suggest that only negligible polarisation is introduced by the interstellar medium. It can be shown that the polarisation of the scattered stellar light in the Earth's atmosphere close to the star is equal to the intrinsic polarisation of the stellar light independent of the scattering mechanism considered, since the scattering takes place primarily through small angles (Le Borgne et al. 1986). Likewise, we expect the polarised flux due to stellar light scattered in the telescope to be very small. Therefore we can assume that  $Q_{sc} \approx 0$  and  $U_{sc} \approx 0$ .

The observations were done in the absence of moonlight. Therefore, the sky background can be disregarded as a source of polarised light, i.e., we set  $Q_{bg} = 0$  and  $U_{bg} = 0$ .

The fact that we could not observe polarimetric standards in any of the runs prevented us from having good estimates of the polarisation introduced by the telescopes and the optics. However, there is no evidence of such polarised light, in the regions where we detect scattered light towards our target stars, in the images of the template stars. This strongly supports our conclusion that polarised flux introduced by the telescope and the optics can be neglected, as well as the presence of a strong, polarised background flux.

Finally, the use of a coronagraph eliminates the direct stellar light, i.e.,  $I_* = 0$ . Thus, we have

$$\begin{cases} I_{sh} = I_m - I_{sc} - I_{bg} \\ Q_{sh} = Q_m \\ U_{sh} = U_m, \end{cases} \quad (2)$$

where  $I_{bg}$  accounts for the sky background light, which must be subtracted during the reduction process.

The polarised flux is expressed then as

$$P_m = P_{sh} = \left( Q_m^2 + U_m^2 \right)^{1/2}. \quad (3)$$

We introduce the measured normalized Stokes parameters to emphasize the polarised scattered light. They, along with the measured polarisation degree, are given by

$$\begin{cases} q_m = Q_m/I_m, \\ u_m = U_m/I_m, \\ p_m = \left( Q_m^2 + U_m^2 \right)^{1/2} / I_m, \end{cases} \quad (4)$$

and the intrinsic polarisation degree of the light scattered in the circumstellar medium is given by

$$p_{sh} = \frac{\left( Q_{sh}^2 + U_{sh}^2 \right)^{1/2}}{I_{sh}} = \frac{\left( Q_m^2 + U_m^2 \right)^{1/2}}{I_m - I_{sc} - I_{bg}}. \quad (5)$$

The measured polarisation degree ( $p_m$ ) only provides a lower limit for the polarisation of the stellar light scattered in the circumstellar medium. The intrinsic polarisation degree ( $p_{sh}$ ) gives the actual value for the polarisation but it must be cautioned that it relies on the more or less uncertain subtraction of the stellar PSF (see below). The polarisation angle is obtained from

$$\theta_{sh} = \frac{1}{2} \arctan \left( \frac{U_m}{Q_m} \right). \quad (6)$$

In the case of observations taken at three polarisation angles, the measured Stokes parameters are derived from the set of images in the following way,

$$\begin{cases} I_m = \text{Frame}(0^\circ) + \text{Frame}(90^\circ) \\ Q_m = \text{Frame}(0^\circ) - \text{Frame}(90^\circ) \\ U_m = 2 \times \text{Frame}(45^\circ) - \text{Frame}(0^\circ) - \text{Frame}(90^\circ). \end{cases} \quad (7)$$

The most arduous task in the data reduction, and probably the one introducing the largest uncertainties, is to obtain  $I_{sh}$ . Apart from subtracting the sky background component ( $I_{bg}$ ), it requires the subtraction of the direct stellar light scattered in the Earth's atmosphere ( $I_{sc}$ ) using the PSF of the observed template star. This procedure is not straightforward, and it is discussed at some length in Paper I. We estimate that the location of the scattered emission, in particular the location of the shells, is not affected by the PSF subtraction. The unreduced data already allow to pinpoint the positions of the shells, confirming that the PSF subtraction procedure does not produce any displacement of the observed scattered light. The total intensity of the scattered emission is uncertain by  $\approx 15\%$  due to the PSF subtraction (see Fig. 1 in Paper I).

The template star subtracted images showing the total intensity of the scattered light ( $I_{sh}$ ) have been edited. Black spots of different sizes are used to blank out the central regions of the images where the mismatch of the target and template PSFs, along with the large intensity gradients, make it impossible to follow any scattered light. For homogeneity reasons, we have done this in the same way for all images shown in this paper. In most observations, the Lyot stop turned out to work inefficiently, yielding highly saturated stripes along two orthogonal directions in the total intensity images. We have lowered the effect of these stripes in the final images of  $I_{sh}$  by replacing them with azimuthally-averaged radial profiles with added Poisson-noise. Therefore, the scattered light detected in the various images is not reliable along these two directions.

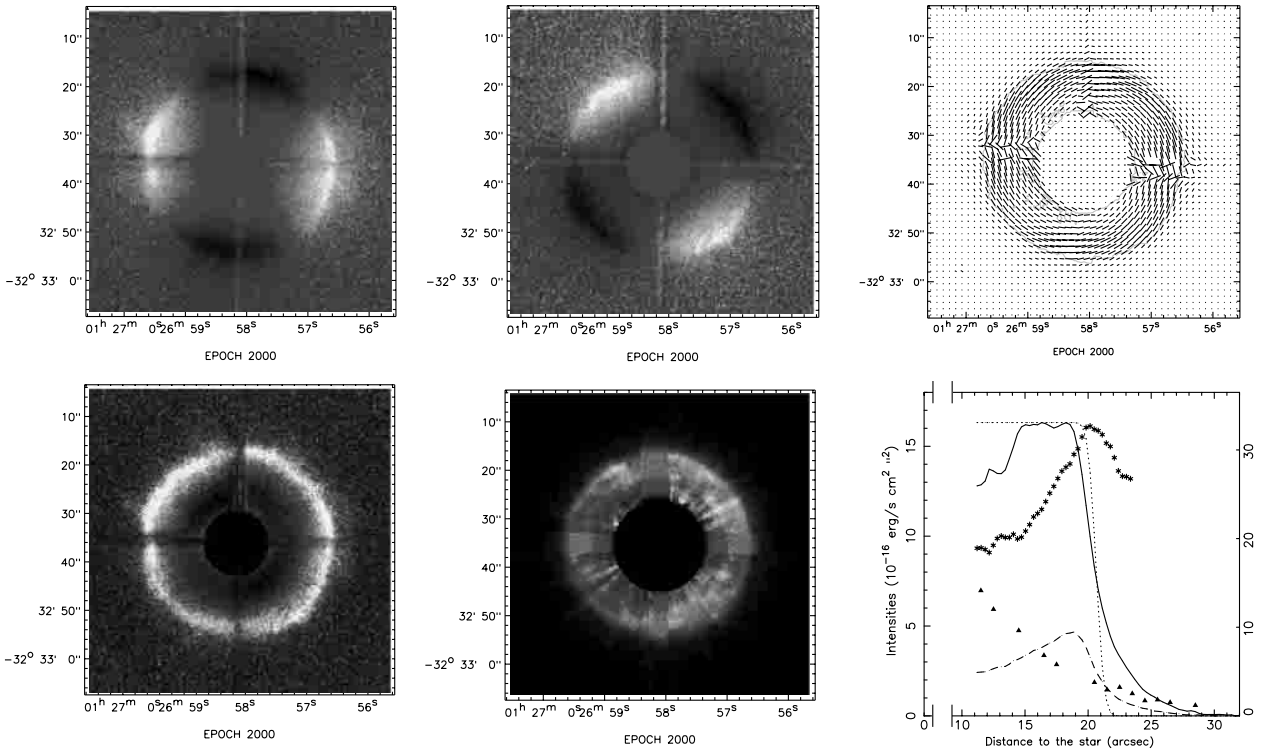


**Fig. 1.** Images showing the polarimetric information in the F77 filter of the light scattered in the circumstellar medium around R Scl. *Upper left panel:* measured normalized Stokes  $q_m$ . *Upper middle panel:* measured normalized Stokes  $u_m$ . *Lower left panel:* measured polarisation degree  $p_m$ . *Lower middle panel:* brightness distribution of the scattered light  $I_{sh}$ . *Upper right panel:* vector map showing the shell polarised intensity ( $P_{sh}$ ) and polarisation angle ( $\theta_{sh}$ ) averaged over square-boxes of  $1''.3$  (the total intensity image is shown as a grey contour). *Lower right panel:* AARP of the polarised intensity ( $P_{sh}$ ; dash-dot line), total intensity ( $I_{sh}$ ; solid line) and polarisation degree ( $p_{sh}$ ; asterisks) of the scattered light. A fit of a step function, convolved with the seeing Gaussian, to the total intensity has been added (dotted line). The AARP of the CO( $J = 3 \rightarrow 2$ ) radio emission seen towards this star (Olofsson et al. 1996) is included for comparison (triangles). The CO peak value, which is reached inside the region probed by these observations, has been normalized to the plateau value of the fit to the total scattered intensity.

## 4. Imaging of circumstellar polarised light

### 4.1. Results towards R Scl

The images in the F77 (Fig. 1) and F59 (Fig. 2) filters of the circumstellar scattered light around R Scl display the measured Stokes parameters ( $q_m$ ,  $u_m$ ), the polarisation degree ( $p_m$ ), as well as the distribution of the total intensity ( $I_{sh}$ ). The  $q_m$ ,  $u_m$ , and  $p_m$  data, in both filters, reveal geometrically thin distributions of scattered polarised light, which are clearly detached from the central star (which lies behind the central mask). On the other hand, the  $I_{sh}$  images show disk-like distributions very similar to those obtained in the direct imaging observations presented in Paper I (the quality of the data is such that we cannot exclude small-scale structure inside the disks). These results are consistent with the presence of a hollow (meaning depleted of gas and/or dust inside a certain radius), spherically symmetric, detached shell around R Scl. Photons scattered along any line-of-sight passing inside the shell outer radius contributes to the observed total intensity, which is therefore detected as a disk-like structure. On the contrary, only those photons which are scattered nearly perpendicularly towards us produce polarised light. This  $90^\circ$  scattering takes place most effectively in the 2D-cut of the spherical shell which is contained in the plane of the sky through the star, and hence, ring-like

structures, such as those exhibited by the Stokes and polarisation degree images, result. Thus, the imaging polarimetry observations effectively reveal the spatial structure of the scattering medium. They allow a determination of the shell inner radius (see Sect. 5.3), which is not measurable in observations of scattered light using direct imaging techniques.

Some quantitative results obtained from these images are also shown in Figs. 1 and 2. The vector maps show the polarised intensities ( $P_{sh}$ ) and polarisation angles ( $\theta_{sh}$ ) at different positions around the star. In both filters there is a centre-symmetric polarisation pattern, typical of isotropic illumination from a central point source.

The azimuthally averaged radial profiles (AARPs) of the  $I_{sh}$  images are relatively constant in both filters, i.e., at both wavelengths the scattered light shows a uniform-intensity brightness distribution. The AARP of  $I_{sh}$  in the F77 filter image extends to an outer radius of  $20''.8$  (corresponding to  $1.1 \times 10^{17}$  cm at the adopted stellar distance of 360 pc). The outer radius is defined as the half power radius of a step function (convolved with the seeing Gaussian) fitted to the observed radial profile (this smoothed function was introduced in Paper I to provide a size estimate, as well as to show that the gradual brightness decline is not an effect of the seeing). The decrease in the total intensity inwards of  $15''$  is very likely not tracing the scattered

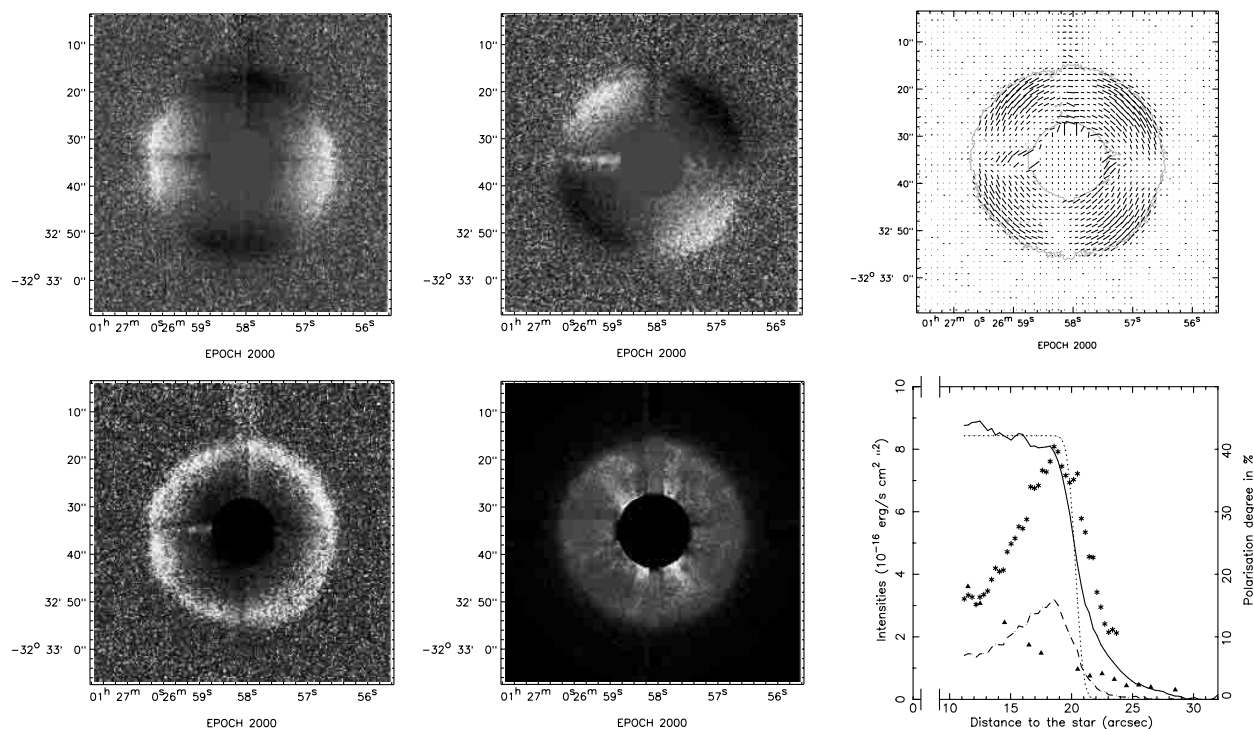


**Fig. 2.** Same as Fig. 1 in the F59 filter.

light, but is probably a by-product of the PSF subtraction procedure, which is less accurate closer to the star. The AARP of  $I_{\text{sh}}$  in the F59 image is constant out to a radius of  $20''.5$ . The errors introduced during the reduction of the images (locations of the stars, PSF subtraction, ...) can account for the small differences in the shell outer radii ( $\lesssim 1''$ ) as derived from the observations in both filters here and from the direct images in Paper I. CO radio line maps towards this star marginally resolve a tentative detached shell (Olofsson et al. 1996), with a peak intensity radius that is a factor of two smaller ( $\approx 9''$ ) than the shell observed in the scattered light. The radial distribution of the CO( $J = 3 \rightarrow 2$ ) intensity, obtained with a spatial resolution of about  $10''$ , is shown in arbitrary units for comparison.

The total fluxes of the circumstellar scattered light are given in Table 2. They are, in both filters, derived from a step-function fit to the AARPs. These values are 0.8 and 0.7 times the total fluxes found in the F77 and F59 filter observations presented in Paper I, respectively. The uncertainties in the indirect calibration of our data in this paper and in Paper I are such that these differences are well accounted for. We estimate the values presented here to be accurate, on an absolute scale, to within a factor of three (see Sect. 2.3).

The AARPs of  $P_{\text{sh}}$  show that the scattered polarised flux increases outwards, peaking at positions which coincide with the outer radii derived from the AARPs of  $I_{\text{sh}}$ . The rise is followed by a steep decline, which reproduces relatively well, in both filters, the decrease in total intensity outside the shell. The polarised fluxes are given in Table 2, and they are uncertain by a factor of about three.

The R Scl data are of limited S/N-ratio and this produces problems when producing images of the intrinsic circumstellar

polarisation degree ( $p_{\text{sh}}$ ), since this involves division of frames. To overcome this problem, we obtained the AARPs of the polarisation degree by direct division of the AARPs of  $P_{\text{sh}}$  and  $I_{\text{sh}}$ . This provides values for the polarisation degree which are independent of the inaccurate data calibration. We have excluded the outermost points where the spread in the data results in highly uncertain values. The polarisation degree in the F77 filter reaches a maximum of about 33% at a distance of  $20''.2$  from the star. In the F59 filter the polarisation degree rises to 40% at  $18''.6$ . The polarisation degree maxima agree well in radius with the outer radii of the total scattered intensities. There is only a weak dependence of the polarisation on wavelength. Since the detached shell lies at  $\approx 20''$  from R Scl, we estimate that there are no substantial effects on the values of  $p_{\text{sh}}$  due to the inaccuracy of the PSF subtraction. In any case, a lower limit to the shell polarisation degree is given by the measured polarisation degree ( $p_{\text{m}}$ ) which peaks at a value of  $\approx 20\%$  in both filters.

#### 4.2. Results towards U Ant

The polarimetric images of U Ant showing  $q_{\text{m}}$ ,  $u_{\text{m}}$ , and  $p_{\text{m}}$  in the F77 filter (Fig. 3) and in the F59 filter (Fig. 4) reveal ring-like brightness distributions in scattered light, which are clearly detached from the star. The image showing  $I_{\text{sh}}$  in the F77 filter exhibits a fairly uniform disk which is somewhat limb-brightened. In the F59 filter, the presence of multiple shells can be discerned. These latter images reproduce fairly well, in both filters, the brightness distributions observed in the direct images of U Ant presented in Paper I. Of particular interest is the mismatch in position between the peaks of polarised intensity (marked as dashed circles on the total intensity images) and the

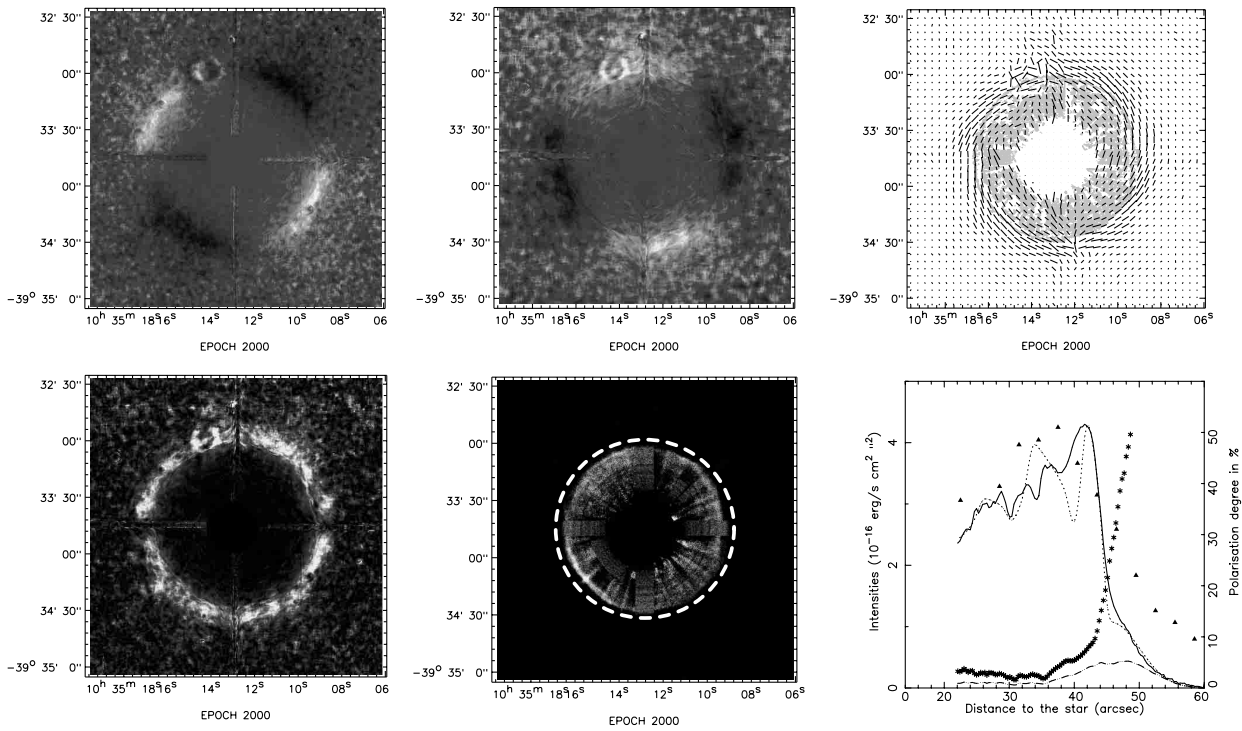


**Fig. 3.** Images showing the polarimetric information in the F77 filter of the light scattered in the circumstellar medium around U Ant. *Upper left panel:* measured normalized Stokes  $q_m$ . *Upper middle panel:* measured normalized Stokes  $u_m$ . *Lower left panel:* measured polarisation degree  $p_m$ . *Lower middle panel:* brightness distribution of the scattered light  $I_{sh}$ . The dashed circle marks the mean position of the maximum reached by the polarised flux. *Upper right panel:* vector map showing the polarised intensity ( $P_{sh}$ ) and polarisation angle ( $\theta_{sh}$ ) averaged over square-boxes of  $3''.8$  (the total intensity image is shown as a shadow). *Lower right panel:* AARP of the polarised intensity ( $P_{sh}$ ; dash-dot-dot line), total intensity ( $I_{sh}$ ; solid line) and polarisation degree ( $p_{sh}$ ; asterisks) of the light scattered in the envelope. Fits of shell brightness distributions, convolved with the seeing Gaussian, to the total intensity have been added (dotted line; see text for details). The AARP of the CO( $J = 2 \rightarrow 1$ ) radio emission seen towards this star (Olofsson et al. 1996) is included for comparison (triangles). The CO peak value has been normalized to the most prominent peak of the fit to the total scattered intensity.

size of the total intensity distribution. The clearly detached nature of the scattered light (both polarised and total) at a large distance from the star exclude the image reduction process (and in particular the PSF subtraction) as a possible reason for the mismatch.

Some quantitative results from these images are also shown in Figs. 3 and 4. In both filters the pattern followed by the vector lines is centre-symmetric, typical of a spherically symmetric distribution of material which is illuminated by a central source.

The AARPs towards U Ant appear more complicated than those obtained towards R Scl. In Paper I we tentatively introduced four circumstellar shells around U Ant. The bulk of the scattered light comes from *shell3*, of size  $\approx 43''$ , which coincides with the detached shell seen in the CO radio lines (Olofsson et al. 1996). Substantially weaker emission comes from *shell4*, which lies outside *shell3* and appears to be somewhat broader. In addition, two tentative shells (*shell1* and *shell2*) inside *shell3* were introduced to explain the inner peaks in the total intensity distribution (seen primarily in the F59 filter). These components are more uncertain since the images may still contain stellar light close to the star despite the subtraction of the stellar PSF. The best fits to the  $I_{sh}$  AARPs use the four shell brightness distributions (convolved with the

seeing Gaussian) which were employed in Paper I: *shell1* to *shell3* are fitted using brightness distributions which correspond to optically thin, isotropic scattering in geometrically thin shells, while the fainter (and more extended) *shell4* component is fitted using a Gaussian (see more details in Paper I).

We will not make a quantitative study of the two inner shells due to the low S/N-ratios of the images. The two outer components lie at mean radii (of the results in the two filters) of  $\approx 43''$  and  $\approx 46''$ , corresponding to  $1.7 \times 10^{17}$  cm and  $1.8 \times 10^{17}$  cm, respectively, at the Hipparcos distance of 260 pc. The fits also allow a rough determination of the shell widths. For *shell3* we derive a value of  $\approx 3''$  ( $1.2 \times 10^{16}$  cm). In the case of *shell4* the inferred value of  $\approx 10''$  represents the FWHM of the Gaussian fit. Some disagreements between the adopted brightness distributions and the observed AARPs are evident, in particular the widths of the multiple shells. This can be an indication of optical thickness in the scattering process since this would have a tendency to broaden the observed profiles. The total fluxes of the light scattered in the two outermost components are given in Table 2. The values are 2.5 and 2 times the total fluxes found in the direct F77 and F59 filter images presented in Paper I, respectively (which were calibrated using photometric standards). Thus, they are in agreement with the factor of about three in uncertainty which we estimate for

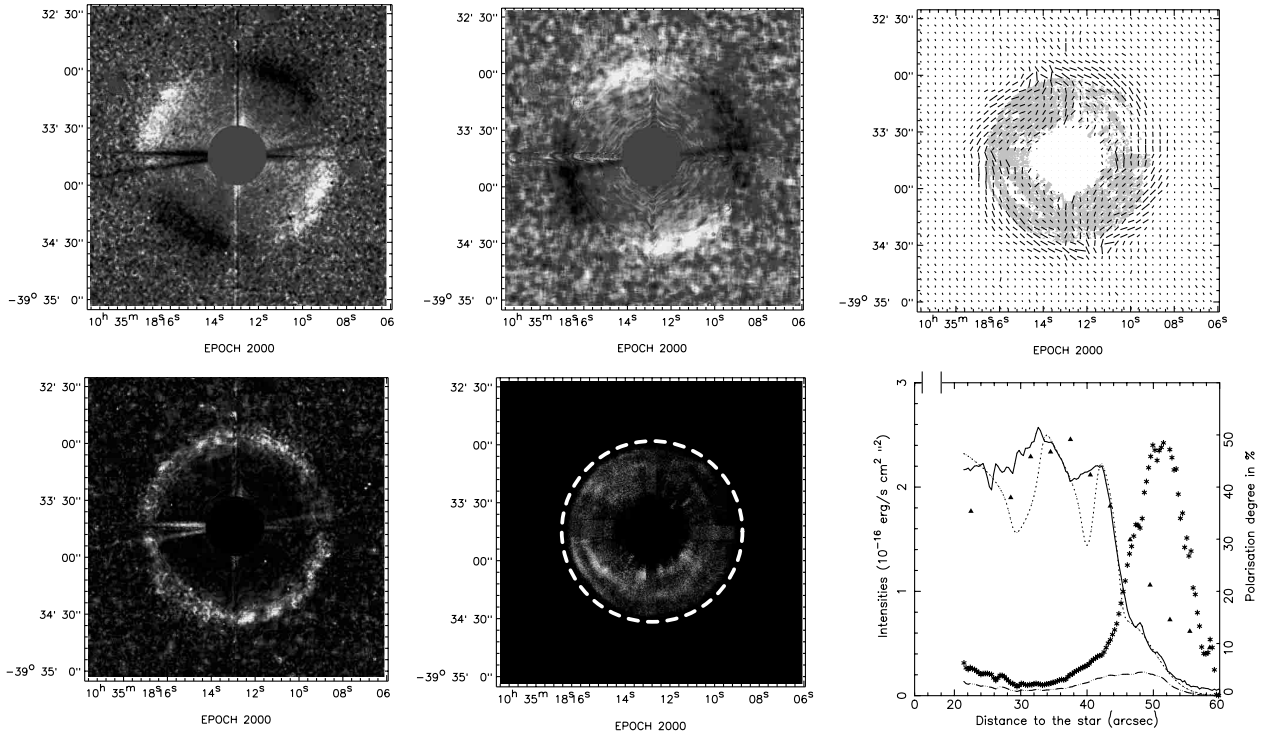


**Fig. 4.** Same as Fig. 3 in the F59 filter.

**Table 2.** Observational results for R Scl and U Ant. The total and polarised scattered fluxes have an uncertainty of about a factor of three, but their ratio is considerably more accurate since the fluxes are obtained from the same images. The ratios of total scattered flux to stellar flux are estimated to be correct to within a factor of five (see text for details).

	Filter	Comp.	$R$	$\Delta R$	Total scattered flux [ $\text{erg s}^{-1} \text{cm}^{-2}$ ]	Polarised scattered flux [ $\text{erg s}^{-1} \text{cm}^{-2}$ ]	CS/S <sup>1</sup>
			[ $''$ ]	[ $''$ ]			
R Scl	F77		20.8		$2.2 \times 10^{-12}$	$5.2 \times 10^{-13}$	$6.7 \times 10^{-4}$
	F59		20.5		$1.1 \times 10^{-12}$	$2.9 \times 10^{-13}$	$7.8 \times 10^{-4}$
U Ant	F77	shell3	43.2	3.2	$1.4 \times 10^{-12}$		
		shell4	46.1	10	$3.3 \times 10^{-13}$		
		all shells			$3.0 \times 10^{-12}$	$3.4 \times 10^{-13}$	$7.1 \times 10^{-4}$
	F59	shell3	43.4	3.5	$7.3 \times 10^{-13}$		
		shell4	46.1	10	$2.2 \times 10^{-13}$		
		all shells			$2.0 \times 10^{-12}$	$1.3 \times 10^{-13}$	$1.1 \times 10^{-3}$

<sup>1</sup> The ratio of total scattered flux and stellar flux.

the crude calibration method used here (see Sect. 2.3). The CO( $J = 2 \rightarrow 1$ ) radial intensity distribution (in arbitrary units) obtained with an angular resolution of about  $15''$  is shown for comparison. It coincides well with the bulk of the scattered emission, and an analysis of the data gives a CO shell radius of  $\approx 41''$  (Olofsson et al. 1996).

In both filters the  $P_{\text{sh}}$  AARPs reach a peak at a distance of about  $47''$  ( $1.9 \times 10^{17}$  cm) from the star, i.e., at the position of *shell4*. This is clearly outside the bulk of the scattered light which is shown in the  $I_{\text{sh}}$  images. We have indicated this by the dotted circles added to these images. Table 2 gives the derived polarised fluxes. The  $p_{\text{sh}}$  AARPs were obtained from direct divisions of the AARPs of  $P_{\text{sh}}$  and  $I_{\text{sh}}$ . The low S/N-ratio of

the U Ant data limits the reliability of the AARPs. They reach  $\approx 50\%$  at  $\approx 50''$  in both filters. This suggests at most a weak dependence on wavelength, the same result as for the scattering around R Scl. In Fig. 3 we have omitted the outermost points in the  $p_{\text{sh}}$  AARPs due to their large variations. The measured polarisation degree  $p_{\text{m}}$  sets a lower limit to the polarisation of the scattered light at a value of  $\approx 10\%$  in both filters.

The fact that the disk-like brightness distributions of the total scattered light lie, in both filters, inside the peak of the ring-like brightness distributions seen in the polarised intensity images is quite remarkable. In Paper I, we suggested the existence of a component (*shell4*) much fainter than, and outside, the main shell (*shell3*). Light scattered in this outer component

was also detected in a continuum filter (Strömgren *b*; Paper I) at a level comparable to those in the F77 and F59 filters. This led us to suggest that the *shell4* component is only due to dust scattering. The results obtained here from the imaging polarimetry observations confirm our suggestion.

## 5. Modelling of the scattered light

### 5.1. The polarising agent

The observation of scattered light in filters containing intrinsically strong lines has the interpretational disadvantage that the data may contain contributions from scattering by both dust grains and gas atoms (on the other hand, they probe both of these circumstellar media). To estimate the amount of total scattered flux due to each scattering agent is therefore not straightforward. In this respect, imaging polarimetry can provide a way to separate the two components.

Rayleigh scattering by small dust particles results in a polarisation degree which increases significantly for scattering angles close to  $90^\circ$ . The polarisation due to line scattering has in principle the same angular behaviour as in the case of Rayleigh scattering by dust. There are particular processes that may decrease the polarisation of line scattering (the presence of a weak magnetic field (Hanle effect), non-coherent scattering due to collisions, and/or interference of atomic sublevels (Nagendra 1988)), but none of them is expected to have any sizeable effect in our case. However, the estimates presented in Paper I point towards (at least partly) optically thick scattering if the observed intensity is due to line scattering. On the contrary, the dust scattering must occur well within the optically thin regime. Thus, optical depth effects may decrease the line polarisation. Dust and line scattering differ in one important aspect. The former has a large forward scattering efficiency which is not present in the latter.

In the following analysis we will assume that the dust grains are the scattering agent responsible for the bulk of the detected polarised light. In Sect. 6 we will put forward more arguments in favour of this interpretation.

### 5.2. The circumstellar model

#### 5.2.1. The radiative transfer

A modified version of the Monte Carlo scattering code of Ménard (1989) was used to compute model brightness distributions. The code only treats the scattering of stellar photons by dust grains. Thus, information on any possible resonance line scattering by K and Na atoms and on the dust thermal emission is not obtained. The method is in principle simple. A number of photons, emitted by the star, are followed through the dusty CSE, and the new photon paths and Stokes intensities are recalculated after each scattering event. Two-dimensional scattered light images are obtained from the number of photons that escape the CSE, and radial profiles of observed quantities can be derived. In all cases the model results are convolved with a seeing Gaussian of  $1''$ .

#### 5.2.2. The circumstellar envelope

Based on the results from the CO radio line observations and the analysis of the scattered light we assume that the CSEs are spherically symmetric, and that they are detached from the stars. The detached nature is specified in the models by an inner radius  $r_{\text{in}}$  at which the dust number density is  $n_{\text{in}}$ . Both quantities are free parameters in the code. The outer radius  $r_{\text{out}}$  is determined by the fits to the observed total intensity AARPs, which show sharp outer cut-offs (Sect. 4). We have assumed constant mass loss rates during the formation of the shells and uniform expansion, i.e., within the shells the dust density distribution,  $\rho_d(r)$ , follows an  $r^{-2}$ -law. It turned out that the shape of the observed radial profiles of the polarised intensity required a smoother decrease in density inside  $r_{\text{in}}$  than provided by a step function (see discussion in Sect. 5.5). We parametrise this as a  $n_{\text{in}}(r/r_{\text{in}})^\alpha$  density law for  $r < r_{\text{in}}$ . As an example, the density has decreased by a factor of ten (from its value at  $r_{\text{in}}$ ) at  $0.75r_{\text{in}}$ ,  $0.83r_{\text{in}}$ , and  $0.87r_{\text{in}}$  for  $\alpha$  equals 8, 12, and 16, respectively. Very likely, the density structure is more complicated than this, but the available constraints are such that a more detailed analysis is not possible.

#### 5.2.3. The dust properties

The dust optical properties are described by the dust absorption and scattering cross sections, which depend on the grain size distribution and the refractive index of the grains. In order to limit the number of free parameters in the models, we have used a single chemical composition of amorphous carbon grains for the dust population. In this context, Bujarrabal & Cernicharo (1994) presented molecular radio line observations towards R Scl. They found, from a comparison of line intensity ratios with those typical in standard AGB-CSEs, that the chemistry of the detached gas shell around this star is C-rich. We note that the presence of carbon grains other than those of amorphous carbon would to some extent modify, through their different polarising characteristics, the results derived here. The optical constants for amorphous carbon at the wavelengths of interest have been obtained from Rouleau & Martin (1991). The corresponding scattering properties of the grains are derived using Mie theory. The grain size distribution is given by a power law with sharp boundaries, i.e.,  $a^{-\beta}$ , where  $a_{\text{min}} \leq a \leq a_{\text{max}}$ . We have fixed the values for the minimum and maximum grain sizes to  $0.05$  and  $2 \mu\text{m}$ , respectively. The exponent  $\beta$  is used as a free parameter.

#### 5.2.4. The fitting procedure

Since for both R Scl and U Ant the scattering is well within the optically thin regime (see below), the dust density at the inner radius,  $n_{\text{in}}$ , is well constrained by the ratio between observed scattered and stellar flux, while the ratio of polarised flux to total scattered flux, i.e., the polarisation degree, is entirely determined by the scattering properties of the dust grains. Once this fact has been established, the rest of the parameters can be determined without influence of optical depth effects, and independently of the absolute calibration.

We start the modelling procedure by fitting the shape of the AARP of the polarised intensity (the fitting range is chosen to lie around the peak flux), since our basic assumption is that all of the scattered polarised flux is due to dust scattering. In this way all parameters, except  $n_{\text{in}}$ , are determined:  $r_{\text{in}}$ ,  $\rho_d(r)$ , and  $\beta$  (the outer radius is fixed and it is determined by the sharp outer decline of the intensity). The effects of varying these parameters are discussed in Sect. 5.5. Since the total scattered flux and the polarised scattered flux are well calibrated relative to each other, the polarisation degree and the estimate of how much of the total scattered flux can be attributed to dust (assuming that dust scattering is responsible for all the polarised flux) are also relatively accurate. Finally,  $n_{\text{in}}$  is obtained by fitting the ratios (in the two filters) of scattered flux to stellar flux. Therefore, the uncertainty in the estimate of  $n_{\text{in}}$  is at least the factor of five which is derived from this ratio.

### 5.3. Results for R Scl

The scattered light images obtained from a model produce total and polarised brightness distributions similar to those observed using as input data  $r_{\text{in}} = 19''$ ,  $r_{\text{out}} = 21''$ ,  $n_{\text{in}} = 3.8 \times 10^{-10} \text{ cm}^{-3}$ ,  $\alpha = 7$ , and  $\beta = -5.5$ . The total intensity images show uniform, disk-like brightness distributions very similar to the observed ones. The ring-like structures seen in the images of the polarised intensities are also well reproduced in the model. The central region appears hollow in polarised light since only scattering at  $\approx 90^\circ$  polarises the light effectively, and there is very little scattering material inside  $r_{\text{in}}$ .

For a more detailed comparison between the model results and the observational data, we have calculated the AARPs of the total intensity, the polarised intensity, and the polarisation degree convolved with a seeing Gaussian of  $1''$ . The best-fit model profiles in the F77 and F59 filters are shown in Fig. 5. The fits to the AARPs of the polarised intensities are relatively good in both filters. In order to reproduce their shape we allowed for a smoother decrease (rather than instantaneous) in the grain number density inside  $r_{\text{in}}$ . The model total intensity increases inwards in both filters as an effect of forward scattering. Unfortunately, our observations do not probe this inner region, but they seem to indicate a rather uniform total brightness. For a direct comparison of the observed and model total fluxes, the model scattered light has not been considered inside the region which is not probed by the observations (inside  $\approx 10''$ ). The total fluxes derived from the model are lower than the observed ones by about 40% in the F77 filter and 30% in the F59 filter (note that the inward drop of the AARP in the F77 filter is probably an effect of PSF oversubtraction). Under the assumption that only the circumstellar grains polarise the scattered stellar light, about 60% of the scattering in the F77 filter and 70% in the F59 filter is due to the dust. Thus, there is possibly room for other scattering agents.

The computed scattering optical depths are, in the F77 filter,  $3 \times 10^{-4}$  in the tangential direction and  $1.5 \times 10^{-4}$  in the radial direction. In the F59 filter the corresponding values are  $8 \times 10^{-4}$  and  $4 \times 10^{-4}$ . Thus, the dust scattering is optically thin in both filters. The uniform intensity disk appearance is

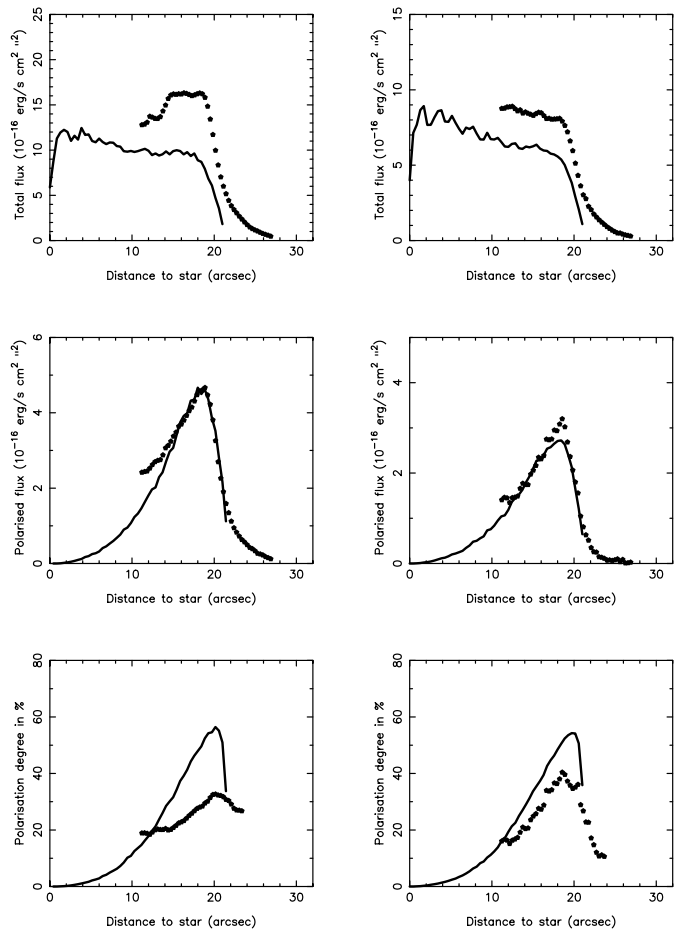


**Fig. 5.** A comparison of the model (solid lines) and observed (dotted lines) AARPs of R Scl in the F77 (left panels) and F59 (right panels) filters. *Upper panel:* total intensity. *Middle panel:* polarised intensity. *Lower panel:* polarisation degree. The model total and polarised intensities are scaled such that the model and observed polarised intensities agree in a region around the peak (see text for details).

therefore attributed to the large forward scattering efficiency, which also masks the geometrical structure. The model results are summarized in Table 3.

The model results are very sensitive to the grain-size distribution, see Sect. 5.5. A very steep decline in grain size is required to fit the observational data ( $\beta = -5.5$ ). Such a steep decline has also been found to best fit polarimetric observations of PPNe (Scarrott & Scarrott 1995; Gledhill et al. 2001). However, grains of size  $< 0.1 \mu\text{m}$  contribute only marginally to the scattering and extinction at optical wavelengths because their effective cross sections are much smaller than their geometrical ones. As a consequence, the maximum contribution to scattering comes from grains in the size-range  $0.1\text{--}0.2 \mu\text{m}$ .

### 5.4. Results for U Ant

The structure of the circumstellar medium around U Ant appears somewhat complicated (this is further discussed in Sect. 6). The presence of one shell (*shell3*) is clearly seen in the total intensity images of the scattered light in both filters, but there may be at least two shells inside this. In the polarised

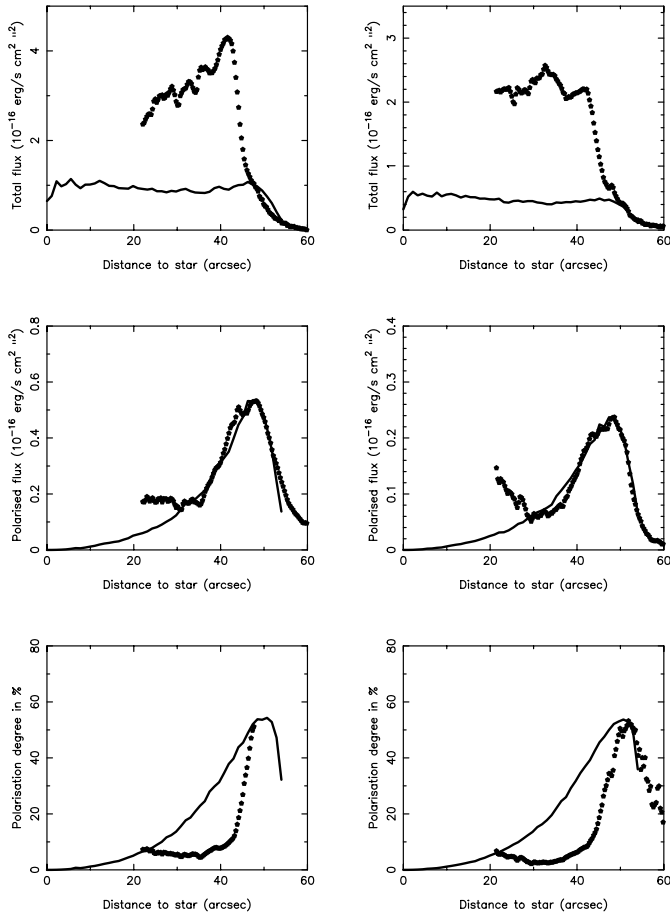


Fig. 6. Same as Fig. 5, but for U Ant.

intensity images only an external component is evident (*shell4*), which is just barely visible in the total intensity data. Therefore, modelling the observed brightness distributions is rather tricky. However, the fact that only the light scattered in *shell4* appears polarised simplifies matter.

The results of the best-fit model to the observed polarised intensities are shown in Fig. 6. The parameters used are  $r_{\text{in}} = 49''$ ,  $r_{\text{out}} = 54''$ ,  $n_{\text{in}} = 1.8 \times 10^{-10} \text{ cm}^{-3}$ ,  $\alpha = 11.5$ , and  $\beta = -5.5$ . The fits are quite good in both filters. However, the model total fluxes (estimated in the region probed by the observations, i.e., outside  $\approx 30''$ ) are very low compared to the observed ones, only 35% of the total scattered flux in the F77 filter and 25% in the F59 filter. This implies that the bulk of the scattered light (*shell1* to *shell3*) is due to another scattering agent. The derived scattering optical depths in the tangential and radial directions are  $3 \times 10^{-4}$  and  $1 \times 10^{-4}$ , respectively, in the F77 filter. At the wavelength of the F59 filter, the corresponding optical depths are  $7 \times 10^{-4}$  and  $3 \times 10^{-4}$ . Like in R Scl, the dust scattering in the circumstellar medium of U Ant is optically thin. The model results are summarized in Table 3.

In order to check this result, we fitted the total scattered light in *shell3* using the scattering code. The result, shown in Fig. 7, is that if the observed light has been scattered by dust grains, it should show clear evidence of polarisation, clearly incompatible with the observations. Dust scattering by grains of different composition, with less effective polarising properties,

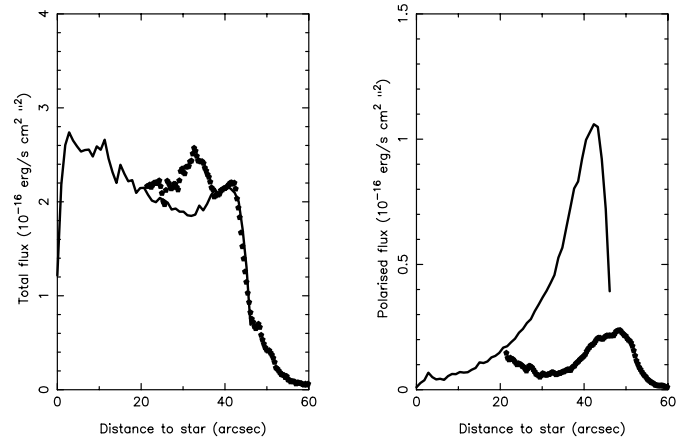


Fig. 7. Model AARPs of the total intensity (left panel) and polarised intensity (right panel) in the F59 filter towards U Ant assuming that the bulk of the stellar light scattered in the *shell3* component is due to dust scattering (dotted lines give observational results).

could explain the fact that the stellar light scattered in *shell3* is not polarised. However, resonance line scattering by K and Na atoms seems to be a more plausible interpretation (see Sect. 6).

### 5.5. Dependence on parameters

We have computed R Scl models with different values for the free parameters in order to investigate their effects on the results, and also to estimate how well these parameters can be constrained. Figure 8 shows the different radial profiles in the F77 filter obtained when  $r_{\text{in}}$ ,  $\rho_d(r)$ , and  $\beta$  (from top to bottom) are changed in the optically thin regime. The outer radius is fixed and it is determined by the sharp outer decline of the intensity. The peak of the polarised intensity provides the point to fit.

The peak radius of the polarised intensity depends sensitively on the inner radius. Thus, this parameter can be determined rather accurately in the modelling, and the uncertainty in the  $r_{\text{in}}$  (and also the  $r_{\text{out}}$ ) estimates are dominated by the seeing ( $\approx 1''$ ). Note here the model results obtained for a CSE which is “attached” to the star. In this case the total and polarised intensities of the scattered light come mainly from line-of-sights close to the star, and the mismatch with the observed profiles is evident.

The shape of the observed polarised intensity AARP could only be fitted with a rather high value of  $n_{\text{in}}$  (since  $r_{\text{in}}$  is fixed by the peak position) for a dust density profile with an instantaneous rise at the shell inner radius (step function profile). Such a high value of  $n_{\text{in}}$  results in scattered flux to stellar flux ratios that are clearly incompatible with the observed ones. An alternative way to fit the shapes of the polarised intensity profiles with lower optical depths, which are consistent with the observed scattered to stellar flux ratios, is to consider density distributions which decrease more gradually inside  $r_{\text{in}}$  (see Sect. 5.2.2). Acceptable fits are obtained for high values of  $\alpha$ , and hence the decrease in density inside  $r_{\text{in}}$  is rather steep.

A large value of  $\beta$  (i.e., less negative) implies an increased importance of larger grains, which makes the scattering

**Table 3.** Model results for R Scl and U Ant (see text for details).

	$R$ ["]	$\Delta R$ ["]	$M_d$ [ $M_\odot$ ]	Filter	Comp.	Total flux [ $\text{erg s}^{-1} \text{cm}^{-2}$ ]	Polarised flux [ $\text{erg s}^{-1} \text{cm}^{-2}$ ]	Scattering by dust <sup>1</sup> [%]
R Scl	20	2	$2 \times 10^{-6}$	F77		$1.3 \times 10^{-12}$	$4.6 \times 10^{-13}$	60
				F59		$7.7 \times 10^{-13}$	$2.6 \times 10^{-13}$	70
U Ant	52	5	$4 \times 10^{-6}$	F77	shell4	$1.1 \times 10^{-12}$	$3.6 \times 10^{-13}$	35
				F59	shell4	$5.0 \times 10^{-13}$	$1.2 \times 10^{-13}$	25

<sup>1</sup> The amount of scattered light attributed to dust based on the polarised emission.

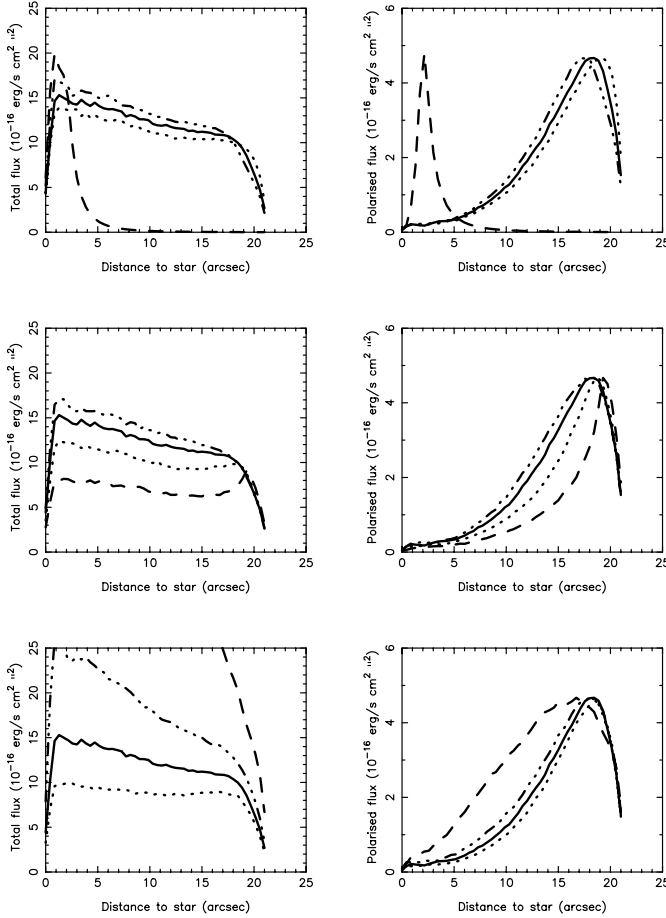


**Fig. 8.** R Scl model AARPs of the total intensities (*left panels*) and polarised intensities (*right panels*) in the F77 filter for different values of the free parameters. *Upper panels*: results for  $r_{\text{in}} = 2''$  (dashed line),  $r_{\text{in}} = 18''$  (dash-dot-dot-dot line),  $r_{\text{in}} = 19''$  (solid line), and  $r_{\text{in}} = 20''$  (dotted line). *Middle panels*: results for inward density power laws of exponent  $\alpha = 8$  (dash-dot-dot-dot line),  $\alpha = 10$  (solid line),  $\alpha = 16$  (dotted line), and  $\alpha = \infty$  (dashed line). *Bottom panels*: results for  $\beta = -4.5$  (dashed line),  $\beta = -5.0$  (dash-dot-dot-dot line),  $\beta = -5.5$  (solid line), and  $\beta = -6.0$  (dotted line) (see text for details).

process less isotropic. This results in high intensities along line-of-sights close to the star as an effect of increased forward scattering. This parameter also affects the wavelength dependence of the polarisation, and it is therefore rather well constrained by the observations in the two filters.

**Table 4.** Observed IRAS fluxes compared to those derived using DUSTY. The model values are separated into the stellar and circumstellar components. The parameters derived from the scattering models are used to describe the circumstellar media around the stars.

	$T_d(r_{\text{in}})$	$F_{12}$ [Jy]	$F_{25}$ [Jy]	$F_{60}$ [Jy]	$F_{100}$ [Jy]
R Scl	star	105	27	5	2
	shell	55	71	16	15
	obs		162	82	54
U Ant	star	182	48	9	3
	shell	44	81	12	29
	obs		168	44	27

### 5.6. Thermal dust emission

A possible way of further constraining the modelling is to see whether the dust shells, which we have derived from the scattering modelling, are able to produce the observed IRAS fluxes, which are due to dust thermal emission. We have estimated their fluxes at 12, 25, 60, and 100  $\mu\text{m}$  using the dust radiative transfer code DUSTY (Ivezić et al. 1999). The parameters derived from the scattering models are used as inputs for the circumstellar medium. For R Scl we used an effective temperature of 2700 K, a luminosity of  $5600 L_\odot$  (Hron et al. 1998), and a stellar distance of 360 pc. In the case of U Ant, 2800 K was adopted and  $5000 L_\odot$  was derived from the measured  $m_{\text{bol}} = 2.58$  (Bergeat et al. 2001) and the Hipparcos distance of 260 pc.

The model results together with the observed IRAS fluxes are given in Table 4. For both stars the derived fluxes are in good agreement with the observed values. The discrepancies are within a factor of three, which is well within our estimated uncertainty of a factor of five for the  $n_{\text{in}}$ 's. Therefore, we tentatively (considering the uncertainties in the calibration of the scattering data) conclude that the same dust component is responsible for the polarised scattered emission in our images and the thermal emission measured by IRAS.

### 5.7. Dust masses and shell sizes

The dust shell masses are estimated using

$$M_d = \frac{16}{3} \pi^2 \rho_{\text{gr}} \int_0^{r_{\text{out}}} \int_{a_{\text{min}}}^{a_{\text{max}}} a^3 n(r, a) da r^2 dr, \quad (8)$$

where  $n_{\text{in}} = \int_{a_{\text{min}}}^{a_{\text{max}}} n(a) da$ , and  $\rho_{\text{gr}}$  is the density of an amorphous carbon grain. We have used  $\rho_{\text{gr}} = 1.85 \text{ g cm}^{-3}$

(Bussoletti et al. 1987) and a distance of 360 pc and 260 pc to R Scl and U Ant, respectively. The derived dust shell masses are  $2 \times 10^{-6} M_{\odot}$  and  $4 \times 10^{-6} M_{\odot}$  for R Scl and U Ant, respectively, and they are uncertain by at least the factor of five uncertainty in the  $n_{\text{in}}$  estimate. Izumiura et al. (1997) calculated the masses of the two dust shells seen in high resolution IRAS images of U Ant. For the inner dust shell (which is likely related to *shell4* in our observations of stellar scattered light) they obtained a value five times higher than our estimate. This difference is partly due to the fact that they used a higher luminosity and a lower effective temperature of the star.

For U Ant we have tried to derive upper limits to the dust shell masses contained in the inner components *shell1*, *shell2* and *shell3*, discernible in the images taken with the F59 filter. The shells positions and widths are taken from the observations presented in Paper I due to the higher S/N-ratios of those images. We assume that an upper limit to the thermal emission by the dust grains in each of these components is given by one quarter of the detected circumstellar  $60\mu\text{m}$  flux, i.e.,  $\approx 8$  Jy. This is a rather conservative estimate. We derive upper limits of  $9 \times 10^{-7} M_{\odot}$ ,  $7 \times 10^{-7} M_{\odot}$  and  $2 \times 10^{-6} M_{\odot}$ , for *shell1*, *shell2* and *shell3*, respectively. Therefore, the dust shell masses are estimated to be lower than in *shell4* by at least a factor of five in the two innermost components and by at least a factor of two in *shell3*.

The modelling of the R Scl data results in a dust shell of radius  $20''$  (or  $1.1 \times 10^{17}$  cm) and of width  $2''$  ( $1.1 \times 10^{16}$  cm). That is, the shell has a small radius/width ratio,  $\Delta R/R \approx 0.1$ , and in this respect it resembles the CO shells seen towards U Cam (Lindqvist et al. 1999) and TT Cyg (Olofsson et al. 2000). Assuming that the CO gas expansion velocity ( $15.9 \text{ km s}^{-1}$ , Olofsson et al. 1996) can be used to estimate the age and the time scale of formation of the dust shell, we obtain an age of about 2200 yr and a formation period of about 220 yr (provided that no effects of interacting winds or shell evolution are present). For U Ant we derive from the scattering model a dust shell width of  $5''$  ( $2.0 \times 10^{16}$  cm) and a radius of  $52''$  ( $2.0 \times 10^{17}$  cm), i.e., it is also geometrically thin ( $\Delta R/R \approx 0.1$ ). Using the CO gas expansion velocity ( $18.1 \text{ km s}^{-1}$ , Olofsson et al. 1996) we estimate age and formation time scales of about 3600 yr and 350 yr, respectively. That is, the two dust shells are characterized by relatively similar time scales.

## 6. Discussion and conclusions

We have confirmed through detailed polarimetric imaging the existence of remarkable circumstellar envelopes around the carbon stars R Scl and U Ant. They have been previously reported in CO radio lines (in the form of detached gas shells; Olofsson et al. 1996), in the case of U Ant in thermal dust emission (in the form of detached dust shells; Izumiura et al. 1997), and in scattered stellar light through direct imaging (Paper I). We have also established that part of the light scattered in these shells is significantly polarised,  $\approx 30$ – $50\%$ . The polarisation data made it possible to establish the spatial structure of the scattering medium, which takes the form of detached, geometrically thin shells. We analysed the polarised scattered light under the assumption that it is entirely due to dust scattering.

The results for U Ant strongly support this, and makes it likely that the same applies to R Scl.

The polarimetry imaging of the light scattered around R Scl and the modelling of dust scattering are consistent with the existence of a thin ( $2''$ , or  $1.1 \times 10^{16}$  cm) shell with a radius of  $20''$  ( $1.1 \times 10^{17}$  cm). The modelling further suggests that as much as 70% of the observed total scattered flux can be due to scattering by dust grains. The required dust mass to achieve this is estimated to be a few  $\times 10^{-6} M_{\odot}$ . Using this dust shell model we are also able to explain the measured thermal dust emission at far-IR wavelengths. However, there appears to be room also for other scattering agents, which produce no polarised emission. We suggest that this scattering is due to K and Na atoms, which have strong resonance lines inside the used filters. If this interpretation is correct, we believe that the most likely explanation to the absence of polarisation in the line scattered radiation is optical depth effects. New data on scattered light in filters not covering these resonance lines and spectroscopic information will shed light on this issue. We note here that in Paper I we concluded that the observed circumstellar scattered flux towards R Scl was too strong for only line scattering (the maximum scattered to stellar flux ratio is given by the ratio of the line width and the filter width). Hence, also this result is consistent with both dust and line scattering, but it depends on the uncertain calibration of the data.

The CO radio line observations towards this star give a different picture, but they are not easily interpreted since the emission may emanate from both a present mass loss envelope and a detached shell (the CO observational results are presented in Olofsson et al. 1996). The angular resolution of the observations do not allow a separation of these two components. We note here that such present mass loss envelopes exist in all the other objects with detached CO shells. We have used the numerical code presented by Schöier & Olofsson (2001) to model the CO line emission. Input data appropriate for a C-rich CSEs were also taken from this paper. It is possible to explain the observed line intensities towards the star with only a present mass loss envelope if the mass loss rate is as high as  $1.1 \times 10^{-5} M_{\odot} \text{ yr}^{-1}$ . However, the observed CO(3–2) radial intensity distribution is much more extended than the model one, and the observed double-peaked CO(3–2) line profile cannot be reproduced. In addition, the magnitude of the mass loss rate is much higher than those provided by other estimates (e.g., Gustafsson et al. 1997), and it is incompatible with the star being an optically bright carbon star. Thus, the CO line emission must have a significant contribution from a detached shell. The inability to separate any present mass loss rate envelope emission from that of the detached shell makes it difficult to estimate the size of the detached CO shell. Olofsson et al. (1996) made a crude estimate assuming that all of the CO radio line emission comes from the detached shell. The result was a shell radius of  $9''$  and an upper limit of  $12''$  to the shell width. The shell radius must be regarded as a lower limit. The observations of Gustafsson et al. (1997), described below, suggests that the CO shell lies outside about  $10''$ . Further modelling of the CO line emission has shown that a dust envelope of the size and mass estimated from the scattering data would under normal circumstances (e.g., with a normal dust-to-gas mass ratio the

estimated dust mass and shell size corresponds to a gas mass loss rate in the range  $(0.5\text{--}1.5) \times 10^{-5} M_{\odot} \text{ yr}^{-1}$  be detected in CO radio line emission (although this depends somewhat on the uncertain kinetic temperature), provided that the CO molecules are not photodissociated (and we know there exist much larger shells than that of R Scl in which the CO has survived, e.g., those of TT Cyg and S Sct). However, it would produce highly double-peaked line profiles in both the CO(2–1) and CO(3–2) lines, and there is no apparent evidence of this. Thus, with some considerable uncertainty, we conclude that the dust shell at  $20''$  contains very little CO gas, and by inference very little gas.

Additional data are available. Detections of emission in radio lines of HCN, CN, and CS are reported for this source (Bujarrabal & Cernicharo 1994; Olofsson et al. 1996). These molecules require high densities and temperatures in order to be excited, and have not been detected in any of the sources with large detached CO shells (Olofsson et al. 1996). It is possible that their emission originates close to the star in a present mass loss wind. Gustafsson et al. (1997) performed spectroscopic observations towards R Scl. They clearly detected KI resonance line scattered light of circumstellar origin, which declines as the third power of the angular distance from the star out to a distance of  $\approx 10''$  (beyond this the emission is lost in the noise). This is consistent with a steady mass loss rate wind extending to about  $10''$ . Using these data they estimate a mass loss rate of about  $10^{-6} M_{\odot} \text{ yr}^{-1}$ . Such an envelope produces much weaker CO radio lines than observed, e.g., only about 25% of the CO(1–0) line intensity is accounted for (using appropriate input data for a C-rich CSE), i.e., the presence of a detached shell is inferred.

Therefore, the data suggest the existence of three different circumstellar components, an inner one due to the present mass loss epoch of the star, a middle one producing the bulk of the CO radio line emission, and an outer one mainly composed of dust. We summarize this in Fig. 9.

The polarimetric imaging of U Ant confirms the existence of multiple shells which scatter the stellar light, see Fig. 9 for a summary. However, only the outermost component, weak in total intensity, is detected in polarised flux, *shell4*. Modelling of the polarised intensities shows that dust scattering is able to explain all of the emission from this outer component, but less than 30% of the total scattered light observed towards U Ant can be accounted for in this way. Either a very different grain composition, without polarising properties, or e.g. resonance line scattering by K and Na atoms provides the bulk of the observed scattered light. The former appears unlikely since the dust component in *shell4* accounts also for the measured IRAS fluxes. A simple analysis in Paper I indicates that the latter is certainly possible. In particular, the different morphological appearances in the two filters can be attributed to different optical depths in the KI and Na D resonance lines, and the AARP in the F77 filter suggests (at least partially) optically thin, isotropic scattering (i.e., scattering without a strong forward efficiency as expected from dust). In favour of this interpretation is also that only the *shell4* component was (marginally) detected in a filter which contains no resonance lines (Paper I).

The CO radio line data of U Ant reveal a detached CO gas shell which coincide spatially with *shell3*

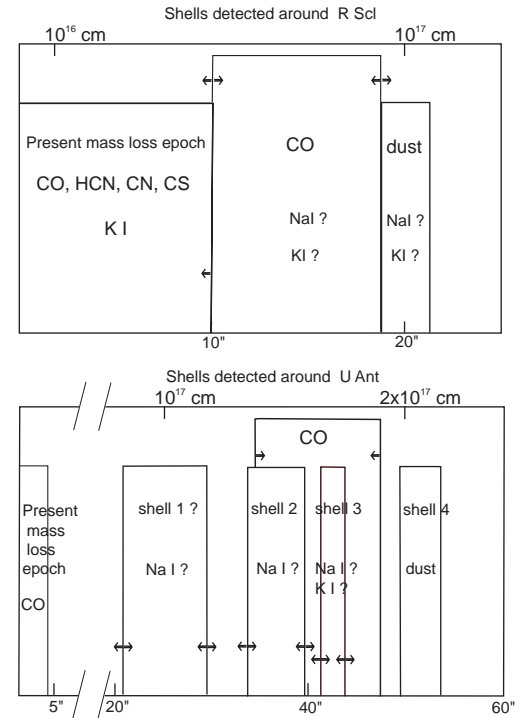


**Fig. 9.** Shells detected around R Scl and U Ant through different observational probes. The arrows indicate the direction of uncertainty in the shells inner and outer radii.

(Olofsson et al. 1996). The angular resolution of the CO observations is rather poor ( $\approx 15''$ ), and the dynamic range is limited. Therefore, we cannot exclude that there exists also CO emission from, at least, *shell2* and *shell4*, but it must be considerably weaker than that of *shell3*. The detailed spatial structure of the CO gas can only be resolved by interferometer observations. Hence, our conclusion is that in the case of U Ant there is good evidence that the dust and the gas has separated.

In both stars we found evidence, stronger in the case of U Ant, of a shell of dust which has separated from the rest of the circumstellar medium. The reason for such a separation is not clear. In the case of U Ant it may be explained by a gas-grain drift scenario. The drift velocity is estimated to be about  $3 \text{ km s}^{-1}$ , a value which is reasonable for a mass loss rate which is estimated to have risen to a value of about  $10^{-5} M_{\odot} \text{ yr}^{-1}$  during the formation of the detached CO shell (Schöier & Olofsson 2001). In the case of R Scl the separation between the gas and dust shell is uncertain. Another possibility is hydrodynamical effects (Steffen & Schönberner 2000; Simis et al. 2001). These would tend to produce differences between the gaseous and the dusty media. Effects of this kind may also lie behind the multiple-shell structure seen towards U Ant.

Clearly, observations made in other filters and using other techniques are needed in order to make progress in this study. Direct and polarimetry imaging performed in high-quality filters containing no resonance lines will supply important information. Spectroscopic observations of the KI and Na D lines will help in disentangling the contributions from dust and gas scattering (see e.g., Maun & Querci 1990; Plez & Lambert 1994; Gustafsson et al. 1997). In high resolution, where the

stellar light is diluted, such observations will also make it possible to observe regions close to the star. R Scl and U Ant are both obvious targets once radio interferometers become available for southern sky objects.

S Sct and TT Cyg, two other bright carbon stars with detected CO gas shells, are good targets for a study similar to that performed here for R Scl and U Ant. However, these stars are in the vicinity of the galactic plane. The presence of numerous field stars and the more extended circumstellar medium around these objects make it more difficult to image the scattered stellar light (though it is feasible, and results will appear in a forthcoming paper). In these cases, it is possible to obtain optical absorption spectra towards background stars lying behind the shells. This novel technique has been recently used by Kendall et al. (2002) to probe the CSE of IRC+10216. They report successful detections of circumstellar KI and Na D resonance lines.

*Acknowledgements.* François Ménard is thanked for allowing us to use his original Monte Carlo scattering code. Financial support from the Swedish Science Research Council is gratefully acknowledged. DGD is grateful for a NOT/IAC graduate study stipend.

## References

- Balick, B. 1987, *AJ*, 94, 671
- Bergeat, J., Knapik, A., & Rutily, B. 2001, *A&A*, 369, 178
- Bujarrabal, V., & Cernicharo, J. 1994, *A&A*, 288, 551
- Bussoletti, E., Colangeli, L., Borghesi, A., et al. 1987, *A&AS*, 70, 257
- González Delgado, D., Olofsson, H., Schwarz, H. E., et al. 2001, *A&A*, 372, 885 (Paper I)
- Gledhill, T. M., Chrysostomou, A., Hough, J. H., et al. 2001, *MNRAS*, 322, 321
- Groenewegen, M. A. T., & de Jong, T. 1994, *A&A*, 282, 115
- Gustafsson, B., Eriksson, K., Kiselman, D., et al. 1997, *A&A*, 318, 535
- Harpaz, A., Rappaport, S., & Soker, N. 1997, *ApJ*, 487, 809
- Hashimoto, O., Izumiura, H., Kester, D. J. M., et al. 1998, *A&A*, 329, 213
- Habing, H. J., te Lintel Hekkert P., & van der Veen, W. E. C. J. 1989, *Planetary Nebulae*, IAU Symp. 131, ed. S. Torres-Peimbert (Dordrecht: Kluwer), 359
- Hron, J., Loidl, R., Höfner, S., et al. 1998, *A&A*, 335, L69
- Ivezić, Ž., Nenkova, M., & Elitzur, M. 1999, *User Manual for DUSTY*, University of Kentucky, Internal Report
- Izumiura, H., Hashimoto, O., Kawara, K., et al. 1996, *A&A*, 315, L221
- Izumiura, H., Waters, L. B. F. M., de Jong, T., et al. 1997, *A&A*, 323, 449
- Kastner, J. H., & Weintraub, D. A. 1994, *ApJ*, 434, 719
- Kendall, T. R., Maun, N., McCombie, J., & Sarre, P. J. 2002, *A&A*, 387, 624
- Kwok, S., Su, K. Y. L., & Hrivnak, B. J. 1998, *ApJ*, 487, 809
- Kwok, S. 2000, *The Origin and Evolution of Planetary Nebulae*, Cambridge Astrophysics Ser. 31 (Cambridge: Cambridge Univ. Press)
- Le Borgne, J. F., Maun, N., & Leroy, J. L. 1986, *A&A*, 168, 211
- Le Borgne, J. F., & Maun, N. 1989, *A&A*, 210, 198
- Lindqvist, M., Lucas, R., Olofsson, H., et al. 1996, *A&A*, 305, L57
- Lindqvist, M., Olofsson, H., Lucas, R., et al. 1999, *A&A*, 351, L1
- Maun, N., & Le Borgne, J. F. 1986, *A&A*, 168, 217
- Maun, N., & Querci, F. 1990, *A&AS*, 86, 513
- Maun, N., & Huggings, P. J. 1999, *A&A*, 349, 203
- Maun, N., & Huggings, P. J. 2000, *A&A*, 359, 707
- Ménard, F. 1989, Ph.D. Thesis, Univ. Montreal
- Nagendra, K. N. 1988, *ApJ*, 335, 269
- Olofsson, H., Carlström, U., Eriksson, K., et al. 1990, *A&A*, 230, L13
- Olofsson, H., Eriksson, K., Gustafsson, B., et al. 1993, *ApJS*, 87, 267
- Olofsson, H., Bergman, P., Eriksson, K., et al. 1996, *A&A*, 311, 587
- Olofsson, H. 1999, *Asymptotic Giant Branch Stars*, ed. T. Le Bertre, A. Lèbre, & C. Waelkens (Astronomical Society of the Pacific), IAU Symp., 191, 3
- Olofsson, H., Bergman, P., Lucas, R., et al. 2000, *A&A*, 353, 583
- Plez, B., & Lambert, D. 1994, *ApJ*, 425, 101
- Raveendran, A. V. 1991, *A&A*, 243, 453
- Rouleau, F., & Martin, P. G. 1991, *ApJ*, 377, 526
- Sahai, R., Trauger, J. T., Watson, A. M., et al. 1998, *ApJ*, 493, 301
- Sahai, R., Hines, D. C., Kastner, J. H., et al. 1998, *ApJ*, 492, L163
- Sahai, R., & Trauger, J. T. 1998, *AJ*, 116, 1357
- Scarrott, S. M., & Scarrott, R. M. J. 1995, *MNRAS*, 277, 277
- Schöier, F. L., & Olofsson, H. 2001, *A&A*, 368, 969
- Schröder, K.-P., Winters, J. M., & Sedlmayr, E. 1999, *A&A*, 349, 898
- Simis, Y. J. W., Icke, V., & Dominik, C. 2001, *A&A*, 371, 205
- Speck, A. K., Meixner, M., & Knapp, G. R. 2000, *ApJ*, 545, L145
- Steffen, M., & Schönberner, D. 2000, *A&A*, 357, 180
- Tamura, M., Hasegawa, T., Ukita, N., et al. 1988, *ApJ*, 326, L17
- Waters, L. B. F. M., Loup, C., Kester, D. J. M., et al. 1994, *A&A*, 281, L1
- Weintraub, D. A., Kastner, J. H., Hines, D. C., et al. 2000, *ApJ*, 531, 401